

UCLA

UCLA Previously Published Works

Title

The structural basis for monoclonal antibody 5D2 binding to the tryptophan-rich loop of lipoprotein lipase

Permalink

<https://escholarship.org/uc/item/03p650j9>

Journal

Journal of Lipid Research, 61(10)

ISSN

0022-2275

Authors

Luz, John G
Beigneux, Anne P
Asamoto, DeeAnn K
[et al.](#)

Publication Date

2020-10-01

DOI

10.1194/jlr.ra120000993

Peer reviewed



The structural basis for monoclonal antibody 5D2 binding to the tryptophan-rich loop of lipoprotein lipase

John G. Luz¹, Anne P. Beigneux², DeeAnn K. Asamoto³, Cuiwen He², Wenxin Song², Christopher M. Allan², Jazmin Morales², Yiping Tu², Adam Kwok², Thomas Cottle¹, Muthuraman Meiyappan⁴, Loren G. Fong², Judy E. Kim³, Michael Ploug^{5,6}, Stephen G. Young^{2,7,*}, and Gabriel Birrane^{1,*}

¹Division of Experimental Medicine, Beth Israel Deaconess Medical Center, Boston, MA, USA, ²Department of Medicine, David Geffen School of Medicine, University of California Los Angeles, Los Angeles, CA, USA, ³Department of Chemistry and Biochemistry, University of California San Diego, San Diego, CA, USA, ⁴Analytical Development, Pharmaceutical Sciences, Takeda Pharmaceutical Company, Lexington, MA, USA, ⁵Finsen Laboratory, Rigshospitalet, Copenhagen, Denmark, ⁶Biotech Research and Innovation Centre (BRIC), University of Copenhagen, Copenhagen, Denmark, ⁷Department of Human Genetics, David Geffen School of Medicine, University of California Los Angeles, Los Angeles, CA, USA

Abstract For three decades, the LPL-specific monoclonal antibody 5D2 has been used to investigate LPL structure/function and intravascular lipolysis. 5D2 has been used to measure LPL levels, block the triglyceride hydrolase activity of LPL, and prevent the propensity of concentrated LPL preparations to form homodimers. Two early studies on the location of the 5D2 epitope reached conflicting conclusions, but the more convincing report suggested that 5D2 binds to a tryptophan (Trp)-rich loop in the carboxyl terminus of LPL. The same loop had been implicated in lipoprotein binding. Using surface plasmon resonance, we showed that 5D2 binds with high affinity to a synthetic LPL peptide containing the Trp-rich loop of human (but not mouse) LPL. We also showed, by both fluorescence and UV resonance Raman spectroscopy, that the Trp-rich loop binds lipids. Finally, we used X-ray crystallography to solve the structure of the Trp-rich peptide bound to a 5D2 Fab fragment. The Trp-rich peptide contains a short α -helix, with two Trps projecting into the antigen recognition site. A proline substitution in the α -helix, found in mouse LPL, is expected to interfere with several hydrogen bonds, explaining why 5D2 cannot bind to mouse LPL.

Supplementary key words antibodies • lipid metabolism • protein structure • triglycerides • X-ray crystallography

The LPL-specific mouse monoclonal antibody 5D2, created by the laboratory of John Brunzell (1–3), has been a key reagent for investigating LPL for more than 30 years. 5D2 was generated by immunizing mice with bovine LPL but binds LPL from multiple vertebrate species (including rat LPL but not mouse LPL) (2, 3). 5D2 was initially used to develop immunoassays for LPL in human plasma (1). Subsequently, the epitope for 5D2 was localized to the carboxyl-terminal domain of LPL (downstream from the larger

N-terminal domain containing LPL's catalytic triad) (3). Nevertheless, 5D2 was shown to block 95% of LPL's catalytic activity against a triolein substrate (4). That observation, together with the observation that 5D2 does not block LPL's activity against a soluble substrate, suggested that 5D2 could bind to lipid-binding sequences in LPL and thereby interfere with lipid delivery to LPL's catalytic domain (4).

Defining the location of 5D2's epitope has had a topsyturvy history. Initially, the laboratory of John Brunzell proposed, based on experiments with a LPL synthetic peptide, that 5D2 binds to LPL residues 423–432 (5), but subsequent studies cast doubt on that finding. For example, Lookene et al. (6) found that mutating two tryptophans (Trps) (W420, W421) in a carboxyl-terminal Trp-rich motif markedly reduced 5D2 binding as well as LPL's ability to hydrolyze the triglycerides in triglyceride emulsion particles. Studies by Williams et al. (7) revealed that mutating W420 and W421 abolished the ability of the carboxyl terminus of LPL to bind lipoproteins. The importance of the Trps for LPL–lipoprotein interactions was confirmed by Goulbourne et al. (8). These studies implied that the Trp-rich loop is relevant to 5D2 binding as well as lipoprotein binding—either directly or indirectly by disrupting the overall conformation of the enzyme.

Soon after Lookene et al. (6) showed that LPL residues W420 and W421 were important for 5D2 binding, Chang et al. (2) found, using competitive immunoassays, that 5D2 bound to a synthetic peptide corresponding to LPL's Trp-rich motif (residues 411–423) but not to the sequences proposed initially by Brunzell's group (residues 423–432). 5D2 did not bind to a synthetic peptide corresponding to the Trp-rich motif of mouse LPL, which contained a Ser-to-Pro substitution at residue 418. Recently, Kristensen et al. (9) demonstrated, using synthetic peptides and surface plasmon resonance (SPR) studies, that 5D2 binds to LPL's Trp-rich motif, and they went on to quantify the impact of each amino acid residue in the Trp-rich loop for 5D2 binding affinity.

This article contains [supplemental data](#).

*For correspondence: Stephen G. Young, sgyoung@mednet.ucla.edu; Gabriel Birrane, gbirrane@bidmc.harvard.edu.



Studies using 5D2 to probe LPL structure have also had a topsy-turvy history. Brunzell's laboratory reported that LPL could be detected with a "single antibody" sandwich ELISA in which 5D2 was used both to capture LPL and to detect the bound LPL (3). That observation led them to infer that LPL must be a homodimer. Additional studies with antibody 5D2 led them to infer that LPL's catalytic activity actually depends on the assembly of LPL into homodimers (3). The concept that LPL was a homodimer had already been proposed (10–12), but the immunological studies by Brunzell and coworkers (3) were crucial for dogmatizing this concept. The notion that LPL is active only as a homodimer was universally accepted (4, 13–15), and newer discoveries in the field were invariably interpreted within the framework of LPL being a homodimer (16, 17). In recent years, however, both of the early inferences from 5D2-based immunoassays—that LPL is a homodimer and that homodimer formation is essential for catalytic activity—have proven to be incorrect. Using 5D2-based ELISAs and density gradient ultracentrifugation studies, Beigneux et al. (18) showed that freshly secreted catalytically active LPL is monomeric. Detection of fresh LPL in a "single-antibody" 5D2 sandwich ELISA was negligible, consistent with LPL being a monomer (18). The fact that freshly secreted LPL, as well as low concentrations of purified LPL, are monomeric was confirmed by highly standardized density gradient ultracentrifugation studies (18).

Subsequent small angle X-ray scattering studies and X-ray crystallography studies (19) revealed that purified LPL, when present at high protein concentrations, assumes a head-to-tail homodimer conformation (19). Two partner LPL monomers interacted reciprocally at a single site; the Trp-rich loop in the carboxyl terminus of one LPL monomer was buried in the catalytic pocket in the N terminus of the partner LPL monomer (19). The same head-to-tail LPL dimer interactions were observed by cryo-EM in large oligomeric helical LPL fibrils (20). This head-to-tail homodimer conformation is incompatible with LPL activity, as it would not allow interactions of lipoproteins with the Trp-rich motif, nor would it allow triglyceride hydrolysis by the catalytic domain (18, 19).

The fact that 5D2 binds to LPL's carboxyl-terminal Trp-rich loop led Kristensen et al. (9) to predict that the binding of 5D2 to LPL would abolish the LPL–LPL interactions observed in the crystal structure and thereby trap LPL in a monomeric conformation. Indeed, purified preparations of LPL, even at high protein concentrations, were monomeric in the presence of 5D2 Fab fragments, and the monomeric LPL remained catalytically active against a soluble substrate (9). Thus, the field's understanding of LPL structure had come full-circle. Older studies with 5D2 were interpreted as showing that LPL is a homodimer and that homodimers are required for catalytic activity (3). The more recent studies with 5D2 revealed that catalytically active LPL is actually monomeric (18) and that 5D2 abolishes LPL's propensity for homodimer formation (9).

Now, three decades after antibody 5D2 was created, two issues require clarification. First, the structural basis for

5D2 binding to the Trp-rich loop in LPL has never been defined, nor have there been insights into why 5D2 fails to bind to mouse LPL. A second issue requiring attention is the role of LPL's Trp-rich loop in binding lipids. The Trp-rich loop is clearly important for lipoprotein binding and triglyceride hydrolysis in the context of full-length LPL (6), but evidence that the Trps are directly involved in lipid binding has been lacking. In the current study, we investigated both issues.

MATERIALS AND METHODS

Production of monoclonal antibody 5D2

The hybridoma for 5D2 was a gift from Dr. John Brunzell (University of Washington). The cells were adapted and cultured in a 50:50 mixture of PFHM II (Gibco) and DMEM (Gibco) media containing 10% FBS (GE Healthcare), 5% L-glutamine, 5% penicillin/streptomycin, and 5% sodium pyruvate. Medium from four T175 flasks (Corning) was harvested every 3–4 days, centrifuged to remove detached cells, and filtered through a 0.22 μ m Stericup filter (MilliporeSigma). Antibodies in the medium were concentrated by precipitation with 50% ammonium sulfate and centrifugation (4,000 *g* for 30 min); the pellet was resuspended and dialyzed against 20 mM sodium phosphate buffer (pH 7.0). After centrifugation (4,000 *g* for 10 min) to remove insoluble material, the supernatant was loaded onto a Protein G–agarose (Sigma Aldrich) column. The column was washed with a minimum of 10 column volumes of 20 mM sodium phosphate buffer (pH 7.0), and antibodies eluted with 100 mM glycine buffer (pH 2.8). The eluate (containing 5D2) was immediately neutralized with 1 M Tris (pH 9.0). The purity of the antibody was established by SDS-PAGE and Coomassie Blue staining; the binding of the antibody to human LPL was established by Western blotting. Protein concentration of the 5D2 antibody was determined by the Bradford protein assay.

Mammalian expression vectors

The complete coding sequence (including the native signal peptide) of human (h), mouse (m), chicken (ck), zebrafish (z), and frog (x) LPL were cloned in frame with a carboxyl-terminus V5 tag into the pcDNA6/V5-His vector (Thermo Fisher Scientific) for expression in mammalian cells under a CMV promoter (21). All plasmids were sequence verified after cloning, and the LPL amino acid sequences started and ended as follows: h, NH₂–MESKALLVLT...HDKSLNKKSG–COOH; m, NH₂–MESKALLLVV...CHDKSLKKSG–COOH; ck, NH₂–MERGRGMGKT...SKENSAHESA–COOH; z, NH₂–MMFNKGRVSS...HGSSFQKQNE–COOH; and x, NH₂–MSSGEFLTFL...NEHAKKKQEW–COOH.

Western blot studies of 5D2 binding to LPL

CHO cells (5×10^6) were electroporated with an expression vector for V5-tagged human, mouse, chicken, zebrafish, and frog (*Xenopus tropicalis*) LPL and then seeded in a 6-well plate. On the next day, total cell lysates were prepared in a buffer [150 mM NaCl, 1.0% IPEGAL CA-630, 0.5% sodium deoxycholate, 0.1% SDS, 50 mM Tris (pH 8.0)]. Proteins were separated by SDS-PAGE and then transferred to a sheet of nitrocellulose membrane. LPL proteins were detected with an IRDye800-conjugated monoclonal antibody against the V5 tag (Thermo Fisher Scientific, 2 μ g/ml) and IRDye680-conjugated 5D2 (4 μ g/ml). The signal for each antibody was quantified with an Odyssey infrared scanner (LI-COR).

Generating 5D2 Fab fragments

5D2 Fab fragments were prepared using the mouse IgG1 Fab and F(ab')₂ fragmentation kit (Thermo Fisher Scientific). Briefly, 5D2 (8 mg/ml) was passed through a Zeba Spin desalting column that was pre-equilibrated with digestion buffer and incubated in the presence of 25 mM cysteine with Ficin-agarose at 37°C for 5 h to create Fab fragments. The Ficin-agarose was removed by centrifugation and nondigested IgG1 and Fc fragments were removed with a Protein A-agarose spin column. Fab fragments were concentrated with a 3K centrifugal filter (Amicon) and further purified by size-exclusion chromatography with a Superdex 200 10/300 column (GE Healthcare) equilibrated with PBS on an ÄKTA Pure HPLC (GE Healthcare) at a flow rate of 0.4 ml/min. The size-exclusion fractions corresponding to the Fab fragments were collected, pooled, and purity verified by SDS-PAGE. The protein concentration of the purified Fab fragments was determined with the BCA protein assay (Thermo Fisher Scientific).

The ability of purified 5D2 Fab fragments to bind to glycosylphosphatidylinositol-anchored HDL binding protein 1 (GPIHBP1)-bound LPL was verified with an LPL-GPIHBP1 “co-plating assay” (21). RJ-1 cells (CHO pgsA-745 cells in which the hamster gene for LPL had been knocked out) (5×10^5 cells) were electroporated with either 0.5 µg of a plasmid for S-protein-tagged versions of wild-type human GPIHBP1 or GPIHBP1-W109S. These cells were then mixed with RJ-1 cells (5×10^5) that had been electroporated with 0.5 µg of a plasmid for V5-tagged human LPL and plated on coverslips in a 24-well plate. After 24 h, the cells were cooled on ice for 10 min and washed twice with PBS/Ca²⁺/Mg²⁺. Cells were then incubated with 20 µg/ml 5D2 Fab fragments in PBS/Ca²⁺/Mg²⁺ for 1 h at 4°C. A control set of cells was incubated with PBS/Ca²⁺/Mg²⁺. The cells were then washed twice with PBS/Ca²⁺/Mg²⁺ and processed for immunocytochemistry. Cells were fixed with 3% paraformaldehyde (PFA) for 15 min, permeabilized with 0.2% Triton X-100 for 5 min, and blocked with 10% donkey serum in PBS/Ca²⁺/Mg²⁺ for 1 h. Cells were then incubated overnight at 4°C with a goat polyclonal antibody against the S-protein tag (Abcam, 1:800). The control set of cells that were not incubated with 5D2 Fab fragments were incubated overnight at 4°C with a mouse monoclonal antibody against the V5 tag (Thermo Fisher Scientific, 1:50). Cells were then incubated for 30 min with an Alexa 488-conjugated donkey anti-mouse IgG (LI-COR Biosciences, 1:800) and an Alexa 568-conjugated donkey anti-goat IgG (LI-COR Biosciences, 1:800). After washing, the cells were fixed with 3% PFA for 15 min and stained with DAPI to visualize DNA. Images were recorded with an LSM 700 confocal microscope on an Axiovert 200M stand and processed with Zen 2010 software (all from Zeiss). The exposure conditions for each construct were identical. These studies (supplemental Fig. S1) showed binding of the 5D2 Fab fragments to GPIHBP1-bound LPL on the surface of cells.

Assessing the impact of a serine-proline interchange at LPL amino acid 418 on 5D2 binding

A point mutation (p.S418P) was introduced into a V5-tagged human LPL expression vector with the QuikChange site-directed mutagenesis kit (Agilent Technologies). The primer sequences were: 5'-TTCATACTTCAGTTGGCCTGACTGGTGGAGCAGT-3' and 5'-ACTGCTCCACCAGTCAAGCCAACTGAAGTATGAA-3' [underlined nucleotides indicate the location of the missense mutation; bolded nucleotides show sites where several changes were introduced (without changing the amino acid sequence) to optimize oligonucleotide melting temperature]. Using the same methods, a p.P418S point mutation was introduced into an expression vector for V5-tagged mouse LPL. The primer sequences were: 5'-ACTCCTACTTCAGCTGCTCAGACTGGTGAGCAG-3' and 5'-CTGCTCCACCAGTCTGACCAGCTGAAG-

TAGGAGT-3' (underlined nucleotides indicate the location of the missense mutation). Transfected cells were plated onto glass cover slips and were grown in Ham's F-12 medium (Thermo Fisher Scientific) containing 2 mM L-glutamine and 10% (v/v) FBS (HyClone). After 24 h, cells were washed three times (10 min each) with PBS/Ca²⁺/Mg²⁺ and fixed for 15 min in PBS/Ca²⁺/Mg²⁺ containing 3% (w/v) PFA. Cells were permeabilized with 0.2% Triton X-100 in PBS/Ca²⁺/Mg²⁺ for 5 min. After blocking with 10% donkey serum in PBS/Ca²⁺/Mg²⁺ for 1 h, cells were incubated for 1 h at room temperature with an Alexa 647-conjugated antibody against the V5 tag (11.6 µg/ml) and Alexa 488-5D2 (20 µg/ml) in PBS/Ca²⁺/Mg²⁺ containing 3% donkey serum and 0.2% Triton X-100. After washing three times in PBS/Ca²⁺/Mg²⁺ (10 min each), cells were fixed with 3% (w/v) PFA in PBS/Ca²⁺/Mg²⁺ for 15 min and then stained with 10 µg/ml DAPI in PBS/Ca²⁺/Mg²⁺ for 5 min. Cells were then rinsed with PBS/Ca²⁺/Mg²⁺ three times and mounted with ProLong gold antifade mounting media (Thermo Fisher Scientific). Images were recorded with an LSM700 confocal fluorescence microscope (Zeiss) and processed with Zen 2010 software (Zeiss).

Analysis of 5D2-LPL binding by SPR

To define the species selectivity of 5D2, we used a Biacore T200 (GE Healthcare) to measure the real-time binding kinetics of synthetic 14-mer LPL peptides spanning the Trp-rich lipid-binding sequences from six vertebrate species. We immobilized 5D2 (5 µg/ml in 10 mM NaOAc, pH 5.0) on a CM5 sensor chip (GE Healthcare) with *N*-hydroxysuccinimide and *N*-ethyl-*N*-(3-(diethylamino)propyl)-carbodiimide, which yielded a surface density of 1,548 resonance units (RU), corresponding to 10.3 fmol of 5D2/mm². Kinetic rate constants for the LPL synthetic peptides were determined with single-cycle protocols (22); five 2-fold dilutions of the peptide were injected for 200 s without intervening regeneration and followed by a dissociation phase of 2,500 s. Interactions were measured at 40 µl/min in 10 mM HEPES, 150 mM NaCl, 3 mM EDTA, and 0.05% (v/v) surfactant P-20 at pH 7.4 at 20°C. Two consecutive injections with 10 µl of 20 mM H₃PO₄ at the end of each single cycle were used to regenerate the chip. Double blank-referenced data were fit by nonlinear regression to a simple bimolecular interaction model with Biacore T200 Evaluation 3.0 software (22). Association (k_{on}) and dissociation (k_{off}) rate constants, the K_D (k_{off}/k_{on}), as well as the binding capacity (R_{max}) were generated assuming pseudo first-order reaction conditions.

Crystallization of 5D2 Fab with and without an LPL peptide

The apo 5D2 Fab (13 mg/ml) was crystallized in the space group C2 at 18°C by vapor diffusion by mixing 0.1 µl of protein with 0.1 µl of reservoir solution containing 100 mM 2-(*N*-morpholino) ethanesulfonic acid (pH 6.5), 150 mM ammonium sulfate, and 20–24% PEG 4000. The LPL14 peptide (human LPL residues 410–423; KSDSYFSWSDWSS) was synthesized and purified (Tufts University Core Facility). A complex of LPL14 and 5D2 Fab was formed by mixing the peptide (10 mM in DMSO) and 5D2 Fab at a 2:1 molar ratio. Crystals in the space group P2₁ were grown by vapor diffusion at 18°C using a well solution containing 16–22% PEG 3350 and 250 mM sodium thiocyanate. Apo and Fab-LPL14 crystals were cryocooled by immersion in liquid nitrogen after a brief soak in the crystallization solutions supplemented with 25% ethylene glycol.

Data collection, structure determination, and refinement

X-ray diffraction data were collected on the Apo 5D2 Fab crystal to a maximum resolution of 2.25 Å at synchrotron beamline I24 at Diamond Light Source (Dcot, UK). Strong anisotropy and elongated diffraction spots limited the effective resolution to 2.85 Å.

The dataset was processed with XDS (23) and Staraniso (24) in the AutoPROC suite (25) in space group C2. The structure was solved by molecular replacement using Phaser (26) with Protein Data Bank identification number (PDB ID) 5D8J (27) as the search model. The asymmetric unit contained one copy of 5D2 Fab, and the structure was refined using Phenix (28) to an R_{work} and R_{free} of 25.3% and 30.8%, respectively.

Data for the 5D2 Fab–LPL14 complex was collected at the 17-ID-1 beamline at NSLS II (Brookhaven National Laboratory, NY). After analyzing a single crystal by rastering, X-ray diffraction data to 2.74 Å were collected along a screw axis and processed in space group P2₁ with HKL2000 (29). Using Phaser (26), the first of two Fab molecules in the asymmetric unit was found by molecular replacement using the structure of the apo 5D2 Fab as the model. Two of the IgG domains of the second copy were placed in a subsequent round of molecular replacement with the first solution fixed. However, due to the difference in elbow angles, the remaining two Ig domains did not fit the electron density map. Attempts to identify a molecular replacement solution for the remaining two Ig domains (constant) using Phaser and MolRep (30) failed, possibly due to weaker electron density for these domains. As density for several β-strands was apparent in the electron density maps, Buccaneer (31) was used to autobuild several β-strand fragments into the electron density map. The complete structural model was built using COOT (32) and refined with REFMAC5 (33) at 2.71 Å resolution to an R_{work} of 20.8% and an R_{free} of 24.3% (Table 2). Validation of the models was carried out using MolProbity (34).

Preparation of small unilamellar vesicles

To generate small unilamellar vesicles (SUVs), a 25 mg aliquot of 1,2-dimyristoyl-*sn*-glycero-3-phosphocholine (DMPC from Avanti Polar Lipids) dissolved in chloroform was dried under nitrogen gas for at least 4 h. The dried lipid was resuspended in 5 ml of 20 mM potassium phosphate (KPi) buffer (pH 8.0), yielding a lipid concentration of 5 mg/ml. The lipid solution was sonicated with an ultrasonic microtip probe at 50% duty cycle with 30% maximum amplitude for 30 min. The SUVs (~50 nm diameter) were passed through a 0.22 μm filter and equilibrated overnight at 40°C before use in experiments. A 5 mg/ml solution served as the stock SUV solution and was further diluted for experiments.

Samples for optical spectroscopy

LPL14 peptide was dissolved in 20 mM KPi buffer at pH 8.0 to create solutions of 10 μM peptide in the absence and presence of 1 mg/ml SUVs; the total volume of each sample was 3.6 ml. Sample solutions of the model compound *N*-acetyl tryptophanamide (NATA) were also prepared. These NATA solutions contained 30 μM NATA in KPi buffer (pH 8.0) in the presence and absence of 1 mg/ml SUVs. A blank solution of 1 mg/ml SUVs in KPi buffer was also generated. This SUV-only solution was used for background subtraction of the absorbance, fluorescence, and UV resonance Raman (UVR) spectra. All samples containing SUVs (peptide + SUVs, NATA + SUVs, and SUVs-only) were allowed to equilibrate at 37°C for at least 1 h prior to collection of measurements. Peptide and NATA samples that did not contain SUVs were incubated at room temperature for at least 30 min prior to measurements. All reagents (NATA and buffer salts) were purchased from Sigma-Aldrich and Thermo Fisher Scientific.

UV-Vis absorption spectroscopy

The absorption spectra of LPL14 and NATA samples were acquired using an Agilent 8453 UV-Visible absorption spectrometer. The absorption features from LPL14 and NATA were isolated by subtraction of an SUV-only spectrum from the raw spectra of pep-

tide and NATA. The concentrations were determined using the 280 nm molar absorption coefficient, ϵ_{280} , for Trp (5,500 M⁻¹cm⁻¹) and tyrosine (1,490 M⁻¹cm⁻¹) (35). The calculated value of ϵ_{280} for LPL14 was 17,990 M⁻¹cm⁻¹ based on the presence of one tyrosine and three Trp residues. All absorption spectra were acquired using a 1 cm path length.

Steady-state fluorescence spectroscopy

The fluorescence spectra were acquired using a Jobin Yvon-SPEX Fluorolog FL3-11 spectrofluorometer (Horiba). All samples were held in a quartz cuvette sealed with a Teflon cap and maintained at 37°C during collection of the spectra. The samples were excited with 290 nm light along the 2 mm path, and emission was collected along the 10 mm path from 305 to 550 nm. The excitation and emission bandpasses were set to 2 nm. Spectra were collected at 1 nm increments with 0.8 s integration time. Fluorescence spectra of SUV-only and buffer-only samples were also collected, and these background spectra were subtracted from the raw fluorescence spectra of peptide and NATA to eliminate signal from buffer and SUV scattering.

UVR spectroscopy

The UVR Ti:Sapphire laser apparatus has been described previously (36). UVR spectra of LPL14 and NATA were acquired with a 228 nm UV excitation beam. The concentrations of LPL14 were 11 μM and 9 μM in the presence and absence of SUVs, respectively. NATA concentrations were 33 μM and 32 μM in the presence and absence of SUVs, respectively. To isolate signal from LPL14 and NATA, UVR spectra of SUVs-only and buffer-only were also acquired and subtracted to remove contributions from vesicle and buffer scattering. All UVR spectra were collected for 20 min. The UV power at the sample was 1.2 mW and the flow rate was set to 0.16 ml/min to ensure fresh sample with each laser pulse and avoid sample degradation.

Peptide folding

The LPL14 peptide sequence was submitted to the PEP-FOLD3 server (<http://bioserv.rpbs.univ-paris-diderot.fr/services/PEP-FOLD3/>) using default parameters (number of simulations = 100; sort by sOPEP). The top five models were superimposed by secondary structure matching (37) and analyzed in COOT (32).

RESULTS

Binding of 5D2 to LPL

We analyzed, by SPR, the binding affinity of immobilized 5D2 to LPL14 and 14-mer peptides corresponding to the same Trp-rich loop in mouse, bovine, rat, chicken, and megabat (“flying fox,” *Pteropus vampyrus*) LPL. The binding affinity of 5D2 to the human and bovine LPL peptides was very high (K_D of 0.19 and 0.78 nM, respectively) (Table 1, Fig. 1). The binding affinity of 5D2 for the chicken LPL peptide was also very high, despite the fact that 5 of 14 residues differed from the human sequence (Table 1). The binding affinity for the rat LPL peptide was modestly reduced, likely due to a Ser-to-Arg substitution in the Trp-rich loop (Table 1). In an earlier study (9), changing that serine in human LPL (Ser-416) to Ala reduced the binding affinity for 5D2. By SPR, 5D2 did not bind to the Trp-rich peptide from mouse LPL,

TABLE 1. Species selectivity of 5D2 by SPR

Species and LPL Sequence	k_{on} ($10^6 \text{ M}^{-1}\text{s}^{-1}$)	k_{off} (10^{-3}s^{-1})	K_D (nM)	Stoichiometry
Human: 410 KSDSY <u>F</u> <u>W</u> <u>S</u> <u>D</u> <u>W</u> <u>W</u> <u>S</u> 423	5.75 ± 0.001	1.10 ± 0.002	0.19	1.5
Cow: 413 I SDSYF S W S N W WSS 426	1.38 ± 0.004	1.08 ± 0.003	0.78	1.3
Rat: 410 K N S D S Y F R W S D W W S S 423	1.97 ± 0.006	5.89 ± 0.002	2.99	1.3
Mouse: 410 M S D S Y F S W P D W W S S 423	NA	NA	NA	NA
Chicken: 410 E K D T F F S W S D W W S T 423	3.64 ± 0.007	1.23 ± 0.002	0.34	1.2
Megabat: 413 Q S N S Y F S W P S W W H S 426	NA	NA	NA	NA

Kinetic rate constants for the binding of LPL14 peptides to immobilized 5D2 (1,548 resonance units (RU), corresponding to $\sim 10.3 \text{ fmol}/\text{mm}^2$) was determined by single-cycle protocols with a Biacore T200 (Fig. 1). We examined 5D2 binding to 14-amino acid peptides of multiple vertebrate species [human, bovine (cow), rat, mouse, chicken, and megabat (*Pteropus vampyrus*)]. The stoichiometry of binding represents the ratio between immobilized 5D2 and the calculated R_{max} for analyte binding (femtomoles per square millimeter) by fitting the data to a 1:1 binding model. NA signifies “non-applicable” because no binding of the mouse or megabat peptides could be observed at concentrations up to 128 nM. The hot-spot residues for 5D2 binding to human LPL are bolded and underlined ($>1,000$ -fold increase in K_D); other important residues (>50 -fold increase in K_D) are underlined (9). Bolded *red* letters depict amino acid residues that differ from the human sequence.

where Ser-418 is replaced with a Pro (Table 1, Fig. 1). 5D2 also did not bind to the Trp-rich LPL peptide from megabat (Table 1, Fig. 1), which has the same Ser-to-Pro substitution. In earlier SPR studies (9), replacing Ser-418 in human LPL with Ala reduced the affinity of 5D2 binding to a synthetic LPL peptide.

We used Western blotting to assess 5D2 binding to V5-tagged full-length human, mouse, chicken, zebrafish, and frog LPL (Fig. 2). We observed avid 5D2 binding

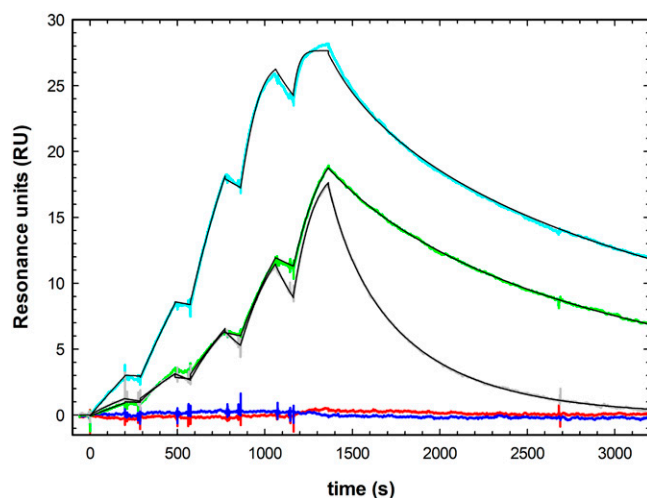


Fig. 1. Species selectivity of 5D2 binding to LPL peptides, as judged by SPR. Shown here are sensorgrams displaying the real-time binding profile of five 14-amino acid LPL peptides to 5D2. The five peptides correspond to the Trp-rich loop in the LPL from different mammalian species. Shown here are the sensorgrams recorded by single-cycle kinetics for 2-fold dilutions (0.5–8 nM) of synthetic peptides for human LPL (cyan), cow LPL (green), and rat LPL (gray), along with the corresponding kinetic fits to the experimental data (thin black lines). Also shown are the sensorgrams for mouse LPL (blue) and megabat (*Pteropus vampyrus*) LPL (red) measured for 2-fold dilutions spanning from 8 to 128 nM. We omitted the sensorgram for chicken LPL because the data were recorded at higher peptide concentrations, complicating direct comparisons to the data generated with human, bovine, and rat LPL.

(relative to the binding of a V5 antibody) to human LPL, but there was no binding of 5D2 to mouse, zebrafish, or frog LPL (Fig. 2). All three of those species contain substitutions in the WSDWW motif (residues 417–421) that is important for 5D2 binding (2, 9). We did detect 5D2 binding to full-length chicken LPL (Fig. 2), but the binding was lower than we would have expected from the SPR studies (Table 1, Fig. 1). This discrepancy suggests that the strength of 5D2 binding to full-length LPL differs from the LPL14 peptide. Such a conclusion is consistent with findings from Kristensen et al. (9), who observed that 5D2 binds to the properly folded carboxyl-terminal domain of human LPL (residues 340–475) with greater affinity than to the LPL14 peptide.

Given that affinity of 5D2 binding to synthetic peptides and properly folded LPL can differ, we examined 5D2 binding to full-length mouse and human LPL. We transfected CHO cells with a V5-tagged full-length mouse LPL vector or with a mutant vector in which Pro-418 had been changed to Ser (the residue found in human LPL). By immunocytochemistry, 5D2 failed to bind to full-length wild-type mouse LPL but bound avidly to the mutant mouse LPL with the p.Pro418Ser substitution (mLPL-P418S) (Fig. 3). In parallel, we tested 5D2 binding to full-length human LPL and a mutant human LPL containing a p.Ser418Pro substitution. 5D2 bound avidly to the wild-type human LPL, but there was no binding to the mutant human LPL with the p.Ser418Pro substitution (hLPL-S418P) (Fig. 3).

Structure of the 5D2 Fab fragment bound to the human LPL14 peptide

We purified Fab fragments of 5D2, verified that they bound GPIHBP1-bound LPL (supplemental Fig. S1), and then used X-ray crystallography to solve the Fab structure, both in the presence and absence of LPL14. The structure revealed a typical Fab tertiary fold comprised of four Ig domains, two from the light chain and two from the heavy

A

h	410	KSDSYF S WSDW SS	423
m	410	MSDSYF S W P DW SS	423
ck	410	E K D T F F S W S D W W T P	423
z	429	E K D T L I S W P-W W N S	441
x	420	E K D S Y F S W S D W F T A	433

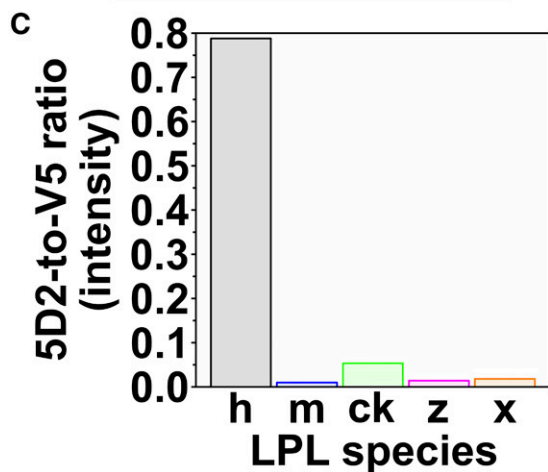
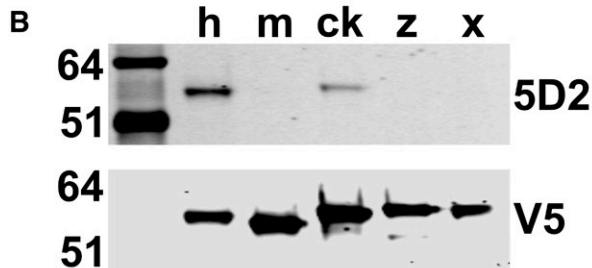


Fig. 2. Binding of 5D2 to LPL from five different vertebrate species. **A:** Multiple sequence alignment of the Trp-rich loop in LPL from human (h), mouse (m), chicken (ck), zebrafish (z), and frog (*Xenopus tropicalis*, x). Residues highlighted in red differ from the human LPL sequence. **B, C:** CHO cells were transfected with expression vectors for V5-tag versions of hLPL (21), mLPL, ckLPL, zLPL, and xLPL. On the following day, total cell extracts were prepared from the transfected cells for Western blot analysis (**B**). After probing the blot with an IR800-labeled anti-V5 antibody (21) and IRDye680-labeled 5D2 (**B**), the signal for each antibody was quantified with an Odyssey infrared scanner (LI-COR). The ratio of the 5D2 signal to the V5 antibody signal was plotted in the bar graph shown in panel **C**.

chain and contained one Fab molecule per crystallographic asymmetric unit. Indexing and scaling of diffraction images for the apo 5D2 structure were complicated by anisotropic diffraction and elongated spots leading to elevated R_{work} and R_{free} factors (Table 2); however, the electron density maps were easily interpretable and allowed for an unambiguous assignment of main-chain and side-chain atoms. Interestingly, the electron density maps for the Apo 5D2 structure showed evidence for two conformations in the side chain of W69 of the heavy chain (part of the antigen binding site) (supplemental Fig. S2). Apart from differences in the IgG hinge angle, the Apo and LPL14-bound 5D2 structures were very similar;

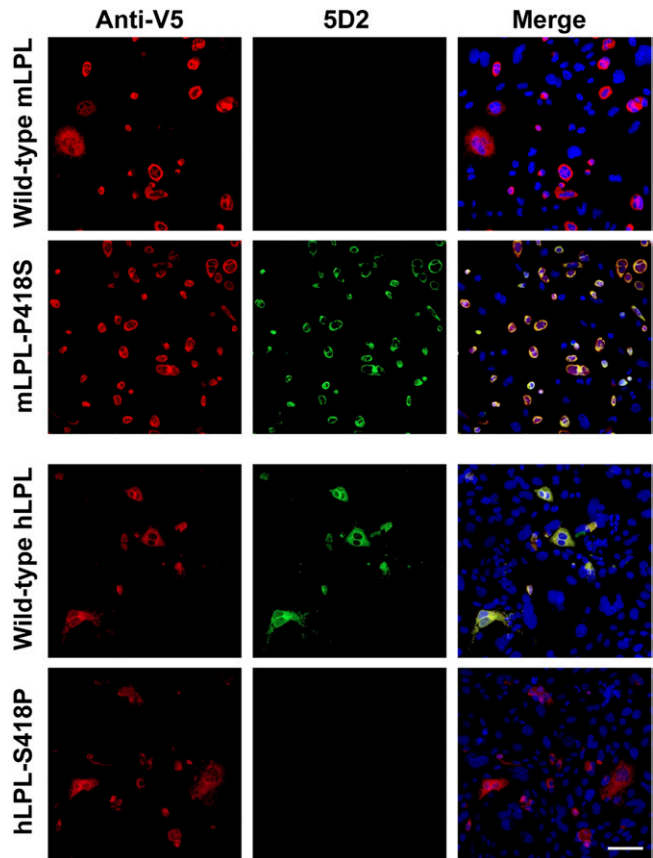


Fig. 3. Introducing a p.S418P mutation into human LPL (hLPL) abolished 5D2 binding, whereas introducing a p.P418S mutation into mouse LPL (mLPL) makes it possible for the protein to bind 5D2. CHO cells were transfected with expression vectors for wild-type mLPL, mLPL-P418S, wild-type hLPL, or hLPL-S418P; all LPL proteins contained a carboxyl-terminal V5 epitope tag. Cells were plated onto glass cover slips. After 24 h, cells were washed three times (10 min each) with PBS/ Ca^{2+} / Mg^{2+} ; fixed with 3% PFA; and permeabilized with 0.2% Triton X-100. Cells were then incubated for 1 h with an Alexa 647-conjugated antibody against the V5 tag (red) and Alexa 488-conjugated 5D2 (green). After washing the cells, they were fixed with 3% PFA, stained with DAPI (blue), and mounted onto slides. Images were recorded with an LSM 700 confocal fluorescence microscope (Zeiss). Scale bar, 50 μm .

the variable domains superimpose with a root-mean-square (RMS) deviation of 0.61 Å in main-chain atom positions (supplemental Fig. S3). The 5D2-LPL14 complex contained two molecules per crystallographic asymmetric unit that were almost identical to each other, with a RMS deviation of 0.31 Å in main-chain atom positions within the variable domains. LPL14 was located in the canonical antigen-binding site at the interface between the heavy and light chains and shaped at its periphery by residues from the complement-determining region (CDR) loops (Fig. 4). The LPL14 peptide was located parallel to the axis of the antigen recognition site, with a hydrophobic face comprised of side chains from F415, W417, W420, and W421 oriented toward the light chain and a polar face (comprised of side chains from S416, S418, D419, and S422) oriented toward the heavy chain (Fig. 5). The N terminus of LPL14 arches over the top of

TABLE 2. Data collection and refinement statistics

	5D2	5D2-LPL
PDB ID	6WT3	6WN4
Wavelength (Å)	0.9686	0.9201
Beamline	DLS, I24	NSLS2, 17-ID-1
Detector	Pilatus3 6M	Eiger 9M
Space group	C2	P ₂ ₁
Cell dimensions		
a, b, c (Å)	138.7, 37.1, 107.9	51.5, 67.6, 129.7
α, β, γ, (°)	90, 126.2, 90	90, 94.4, 90
Resolution (Å)	43.56 – 2.85 (2.91 – 2.85)	29.17 – 2.74 (2.84 – 2.74)
Observed reflections	29,666	120,125
Unique reflections	10,492	23,348
Completeness (%)	97.7 (80.3)	99.3 (93.7)
Redundancy	3.7 (3.6)	5.2 (5.1)
Overall <I/σ(I)>	2.8 (2.1)	10.4 (1.9)
CC _{1/2}	0.976 (0.617)	0.995 (0.729)
R _{pim} (%) ^a	11.6 (40.7)	5.7 (33.0)
R _{work} /R _{free} (%) ^b	25.3/30.8	20.8/24.3
Bond lengths ^c (Å)	0.003	0.003
Bond angles ^c (°)	0.689	1.263
Ramachandran plot (%)	90.0/9.3/0.7	96.0/3.7/0.3
favored/allowed/outliers		

Values in parentheses are for the highest resolution shell. The coordinates for APO 5D2 (PDB ID 6WT3) and 5D2-LPL11 (PDB ID 6WN4) have been deposited in the PDB.

$${}^a R_{pim} = \sqrt{\frac{1}{n-1} \frac{\sum |I - \langle I \rangle|}{\sum I}}$$

Where I is the observed integrated intensity, $\langle I \rangle$ is the average integrated intensity obtained from multiple measurements, and the summation is over all observed reflections.

$${}^b R_{work} = \frac{\sum \|F_o - k|F_c|\|}{\sum F_o}$$

F_o and F_c are the observed and calculated structure factors, respectively, and k is a scaling factor. The summation is over all measurements. R_{free} is calculated as R_{work} using 5% of the reflections chosen randomly and omitted from the refinement calculations.

^cBond lengths and angles are RMS deviations from ideal values.

the heavy chain CDR-H3 loop, with the side chain of D412 in LPL14 folding back to form a hydrogen bond with the guanidinium group of the R121 side chain in the 5D2 heavy chain. A C-terminal α -helical turn in LPL14 (residues 416–421) was nestled into the base of the antigen binding site (Fig. 5).

The interaction of LPL14 with 5D2 is biased toward heavy chain contacts. A total of 193 intermolecular interactions between LPL14 and the heavy chain were identified within a 4.5 Å limit by CONTACT from the CCP4 suite (38), whereas only 37 interactions were identified between LPL14 and the light chain. In addition, 454 Å² of the peptide surface area were buried by the heavy chain, whereas only 131 Å² were buried by the light chain, as determined by the PISA server (39). Electron densities for LPL14 residues K410, S411, and S423 were absent and were not included in the model.

W417 and W421 of LPL14 (within the α -helical turn) extend into a cleft in the antigen-recognition site, with the LPL14 side chains forming edge-to-face π -stacking interactions with light chain W112 (Fig. 6) and additional hydrophobic interactions with the side chains of H54, W69, and H118 of the heavy chain (Fig. 6) and L117 of the light

chain. The indole nitrogen of LPL W417 forms a hydrogen bond with the main-chain carbonyl of heavy chain N122, and the indole nitrogen of LPL W421 forms a hydrogen bond with the backbone carbonyl of W112 of the light chain (Fig. 5). S418 in LPL14 is located within the α -helical turn of the peptide (Fig. 6), and both the main-chain nitrogen and side-chain hydroxyl are within hydrogen bonding distance of the side-chain carboxylate of heavy chain D120 (Fig. 5).

Finding a short α -helix in LPL14 was in line with predictions regarding the structure of the peptide. We submitted the sequence of the LPL14 peptide to the PEP-FOLD3 server (40), and five models were returned. All five had an N-terminal region of undefined secondary structure and a carboxyl-terminal α -helix similar to that observed in the LPL14–5D2 crystal structure (supplemental Fig. S4). The top model was very similar to the crystal structure, with an RMS deviation for backbone atoms of residues in the α -helical region (residues 416–421) of 0.13 Å (supplemental Fig. S4). While the side chains of F415, W417, and W421 were observed as different conformers in the crystal structure and the PEP-FOLD3 models, the α carbons were nearly identical.

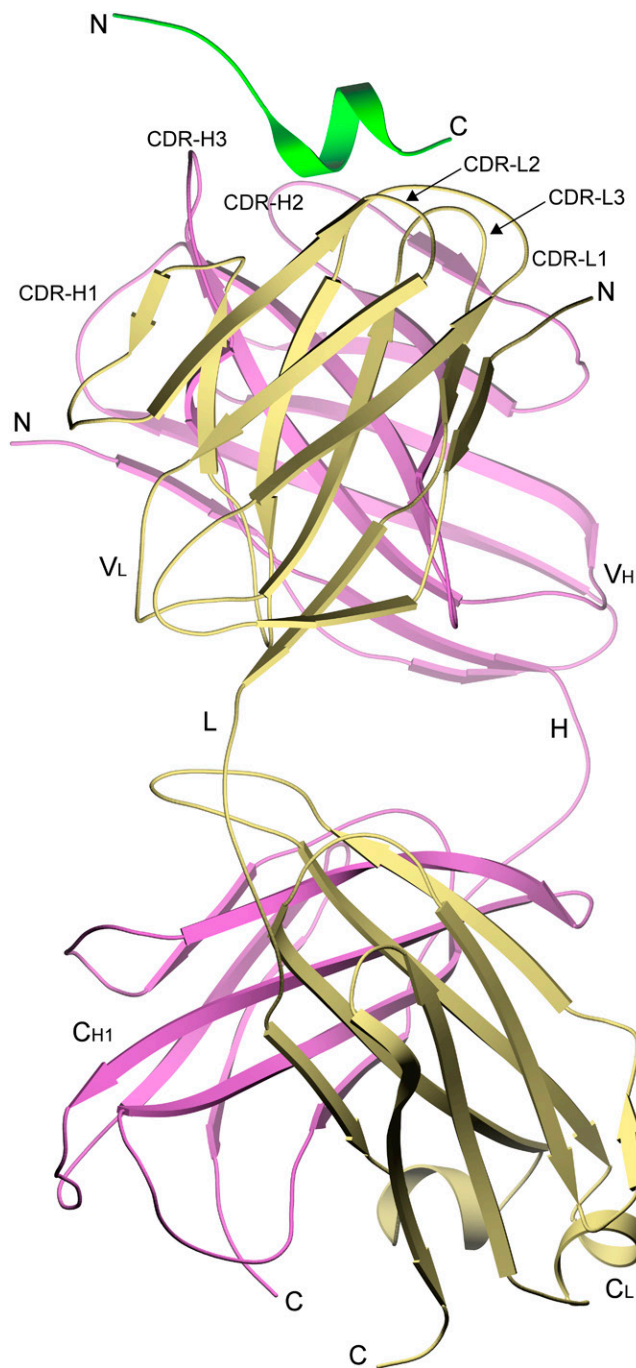


Fig. 4. The crystal structure of the 5D2 Fab–LPL14 complex. α -Helices are depicted as coils; β -strands are depicted as arrows. Heavy chain, purple; light chain, khaki. The LPL14 peptide (KSDSYFSWSDWWSS) is green. This figure was generated using Povscript+ (48) and ray-traced with POVray (<http://www.povray.com>).

There are eight atom pairs in LPL14 and 5D2 common to both molecules in the asymmetric unit that are within hydrogen bonding distance of each other (supplemental Table S1). Of the polar atoms within hydrogen bonding distance, only one pair is found between the LPL peptide and the light chain (LPL W421 indole nitrogen with light chain W112 carbonyl). One pair includes LPL14 main chain atoms and 5D2 side chain atoms, and three pairs include LPL14 side chain atoms and 5D2 main chain atoms. There is one hydrogen bond between backbone atoms of

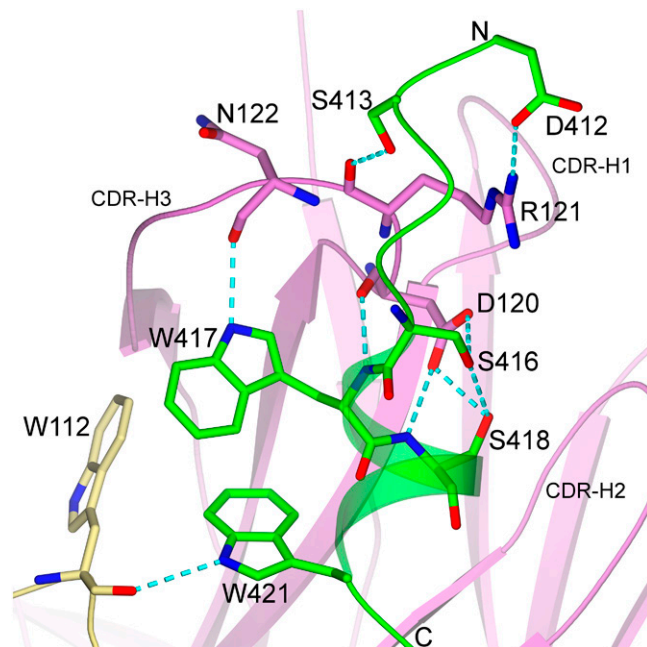


Fig. 5. Antigen binding site of the 5D2 Fab fragment (heavy chain, purple; light chain, khaki) showing hydrogen bonds (dashed cyan lines) between the Fab fragment and the LPL14 peptide (depicted as sticks and colored by atom; C, colored according to chain; O, red; N, blue). The side chains of LPL residues D412, S413, and S416 in the unstructured region of LPL14 and S418 in the α -helical region form a polar interface that is oriented toward the heavy chain (purple ribbons). The N-terminal region of the LPL14 peptide points out of the antigen binding site and arches over the CDR-H3 loop, with LPL D412 forming a hydrogen bond with the R121 side-chain guanidinium of the heavy chain. N ϵ 1 in the five-membered pyrrole ring of W417 and W421 forms hydrogen bonds with the main chain carbonyl groups of N122 (heavy chain) and W112 (light chain), respectively.

both chains—heavy chain D120 carbonyl oxygen to LPL W417 amide nitrogen. The remaining three potential hydrogen bonds are found between pairs of side chain atoms. The network of hydrogen bonds extends across the span of the peptide that was visualized, with the exception of LPL14 residues Y414, D419, and W420 (where the side chains point away from the binding site) and F415 (which cannot form a side-chain hydrogen bond). Of note, framework residue I52 of the heavy chain, which is present in only 0.74% of Kabat database IgG sequences (www.bioinf.org.uk/abs/seqtest.html), forms extensive van der Waals contacts with several LPL14 residues (W417, S418, W421) (Fig. 6). Electron densities for LPL residues K410, S411, and S423 were absent, suggesting that they are not particularly important for 5D2 binding.

Earlier SPR studies found that converting F415, W417, or W421 to an Ala reduced 5D2 binding affinity by more than three orders of magnitude (9). All three aromatic side chains contribute significantly to both the intermolecular hydrophobic packing interactions in the antigen recognition site (Figs. 5, 6) as well as to intramolecular hydrophobic packing that shapes the aromatic face of the peptide. In the same SPR study (9), changing LPL S418 or W420 to Ala decreased binding by 50-fold. The p.Ser418Ala substitution

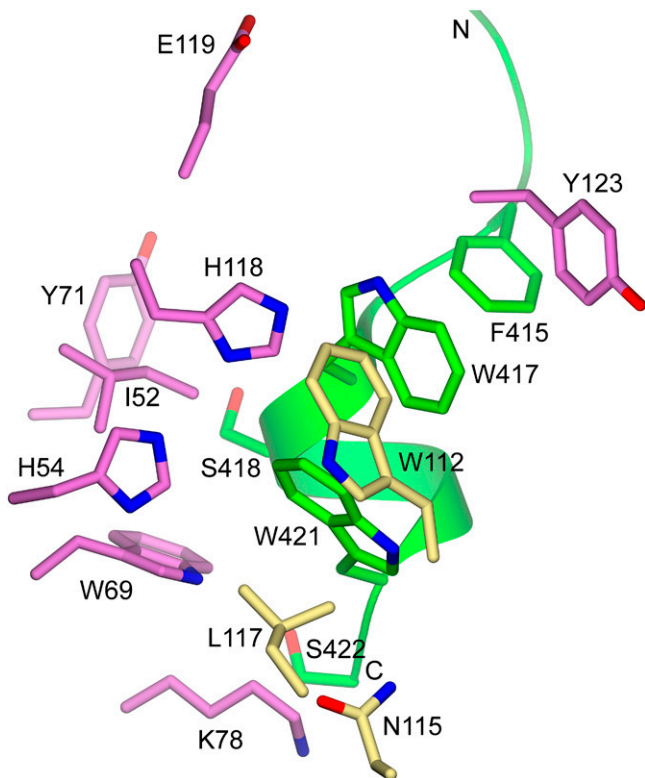


Fig. 6. Hydrophobic interactions of LPL14 residues F415, W417, S418, W421, and S422 (green) with the 5D2 Fab (heavy chain, purple; light chain, khaki). Side chains are represented as sticks and colored by atom (O, red; N, blue; C, colored according to chain). The LPL14 peptide is oriented parallel to the axis of antibody binding. The side chains of F415, W417, S418, and W421 are directed toward the antigen binding site and make hydrophobic contacts predominantly with the 5D2 heavy chain. LPL-S418 makes a hydrophobic contact with W69 and Y71 of the heavy chain, and LPL-S422 interacts with heavy chain K78. There is a minor interaction between LPL W421 and N115 of the light chain. W112 of the light chain interacts with LPL W421 and W417. L117 of the light chain also interacts with LPL W421. The side chain of I52 forms hydrophobic interactions with the side chains of LPL W417 and W421.

would eliminate a hydrogen bond between the side-chain hydroxyl of Ser-418 and the side-chain carboxylate of heavy chain D120 (Fig. 5). The W420A substitution would eliminate hydrophobic packing with the phenyl group of F415.

The conformation of the peptide itself appears to be stabilized by a network of hydrogen bonds, which are conserved between the two copies in the asymmetric unit, except for that formed with the main-chain carbonyl atom of Ser-418 (supplemental Table S2). The carboxyl-terminal α -helical turn is stabilized by main-chain hydrogen bonds formed between residues S416 and W420 and between W417 and W421. Our experiments demonstrated that 5D2 does not bind to mouse LPL (which contains a Pro at residue 418 rather than a Ser), either in the context of the 14-mer synthetic LPL peptide or full-length LPL (Figs. 1, 3). Also, when Ser-418 in human LPL is replaced with a Pro, the binding of 5D2 is abolished (Fig. 3). These observations are explained by our crystal structure. Both the backbone nitrogen and side-chain hydroxyl of Ser-418 in human LPL14 are within hydrogen bonding distance of the side-

chain carboxylate of heavy chain D120 (Fig. 5). Substitution of Ser-418 with a Pro would eliminate crucial hydrogen bonds and introduce a hydrophobic side chain, which would clash with the side chain of D120. Also, the side-chain hydroxyl of Ser-418 is within hydrogen bonding distance to the side-chain hydroxyl of Ser-416, thereby contributing to the internal order of the bound LPL14 structure (Fig. 5). While the Pro at residue 418 interferes with 5D2 binding, there is no reason to suspect that it would interfere with the role of the Trp-rich loop in enzyme function. Interestingly, the PEP-FOLD3 server (40) predicted a short α -helix in the mouse 14-mer LPL peptide, with one side enriched in hydrophobic amino acids (similar to the crystal structure and the PEP-FOLD3 prediction for human LPL14) (supplemental Fig. S5).

The Trp-rich 5D2 peptide (LPL14) interacts directly with lipids

Spectroscopy revealed Trp–lipid interactions between LPL14 and SUV bilayers. The absorption spectrum of LPL14 at 250–320 nm primarily reflects LPL14’s three Trp residues. In the presence of SUVs, the absorption spectrum exhibited a 1 nm red shift from 280 to 281 nm, relative to LPL14 in buffer (Fig. 7). This shift was only observed in LPL14, and not the model Trp compound NATA. This 1 nm shift for LPL14 indicates that the Trp residue(s) are in a more hydrophobic environment in the presence of SUVs (41). This change in environment from aqueous to lipid bilayer is corroborated by fluorescence spectra. The Trp residues in LPL14 exhibited a fluorescence maximum at 358 nm in buffer and shifted to 347 nm in the presence of SUVs, and there was a concomitant increase in the fluorescence intensity (i.e., quantum yield) (Fig. 8). This 11 nm

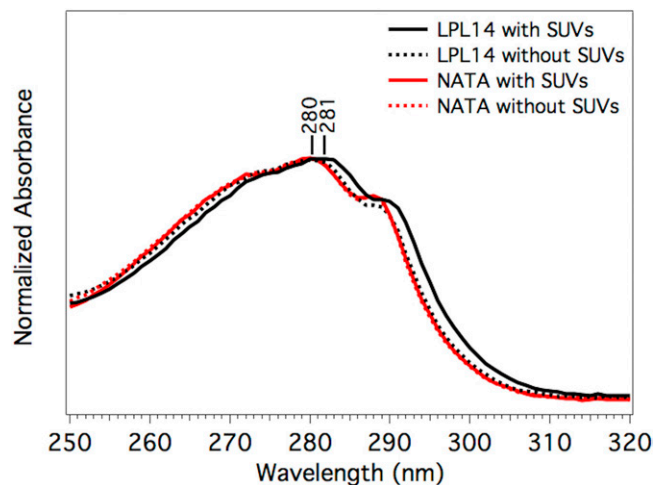


Fig. 7. Absorption spectra of LPL14 in buffer with and without SUVs. Also included are spectra of the model compound NATA in buffer with and without SUVs. Spectra were normalized to equal absorbance at the peak wavelengths of 280 or 281 nm. The spectra of NATA with and without SUVs overlap. Concentrations for LPL14 were 9 μ M (buffer) and 11 μ M (SUVs); concentrations for NATA were 32 μ M (buffer) and 33 μ M (SUVs). The cuvette pathlength was 1 cm. The 1 nm shift in absorption maximum from 280 to 281 nm for LPL14 in the presence of SUVs is consistent with interaction of LPL14 with the lipid bilayer.

blue shift and increase in the quantum yield upon incubation with SUVs indicates that the Trp residues are in a more hydrophobic lipid environment (42).

Vibrational spectroscopy in the form of UVRR supported the absorption and fluorescence findings. UVRR is an ideal tool because excitation at 228 nm enhances the signal from Trp without obfuscation from other residues or buffer. The UVRR bands reflect different properties of the indole side chain. The Trp W7 Fermi doublet band at 1,300–1,400 cm^{-1} is particularly informative because it is a sensitive marker for local hydrophobicity, and the ratio of the peak intensities of 1,366–1,345 cm^{-1} (R_{FD}) increases when Trp is in a hydrophobic environment (36). The R_{FD} value for LPL14 in the presence of SUVs is 1.6, which is significantly larger than the values in buffer and for NATA (Fig. 9). This finding supports the notion that the Trp residue(s) in LPL14 directly interact with the more hydrophobic environment of the lipid bilayer.

DISCUSSION

We defined the structure of 5D2 bound to a 14-mer peptide (LPL14) corresponding to the Trp-rich loop within the carboxyl terminus of human LPL. Eleven of the 14 LPL residues were identified in the electron density map. The carboxyl-terminal portion of the peptide formed a short amphipathic α -helix that was positioned in the cleft of the antigen recognition site, with the hydrophobic face (three

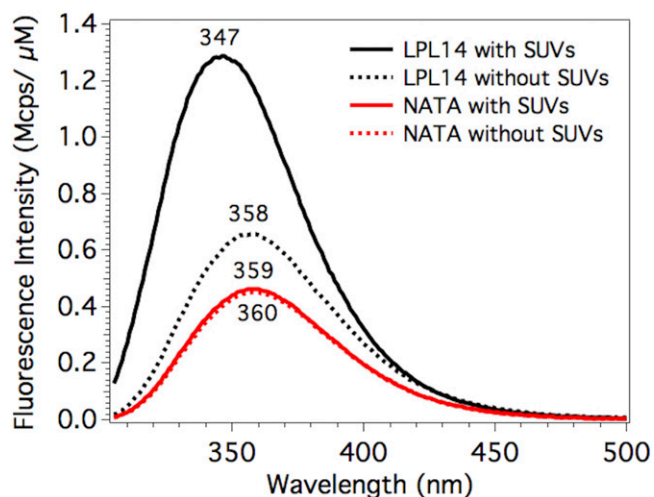


Fig. 8. Fluorescence spectra of Trp residues in LPL14 in buffer with and without SUVs, and the model compound NATA in buffer with and without SUVs. Spectra were normalized to concentrations of LPL14 (9 μM in buffer; 11 μM in the presence of SUVs), and for NATA (32 μM in buffer; 33 μM in the presence of SUVs). The excitation wavelength was 290 nm and was incident on a 0.2 cm pathlength of the cuvette; the emission was collected from 305 to 550 nm along the 1 cm pathlength. The wavelengths of maximum emissions are indicated. The spectra of NATA with SUVs (emission maximum 359 nm) and without SUVs (emission maximum 360) overlap completely. The 11 nm shift from 358 to 347 nm and increase in quantum yield of the Trp fluorescence spectrum of LPL14 in the presence of SUVs indicates that the Trp residue(s) are transferred to the more hydrophobic environment of the bilayer in the presence of SUVs.

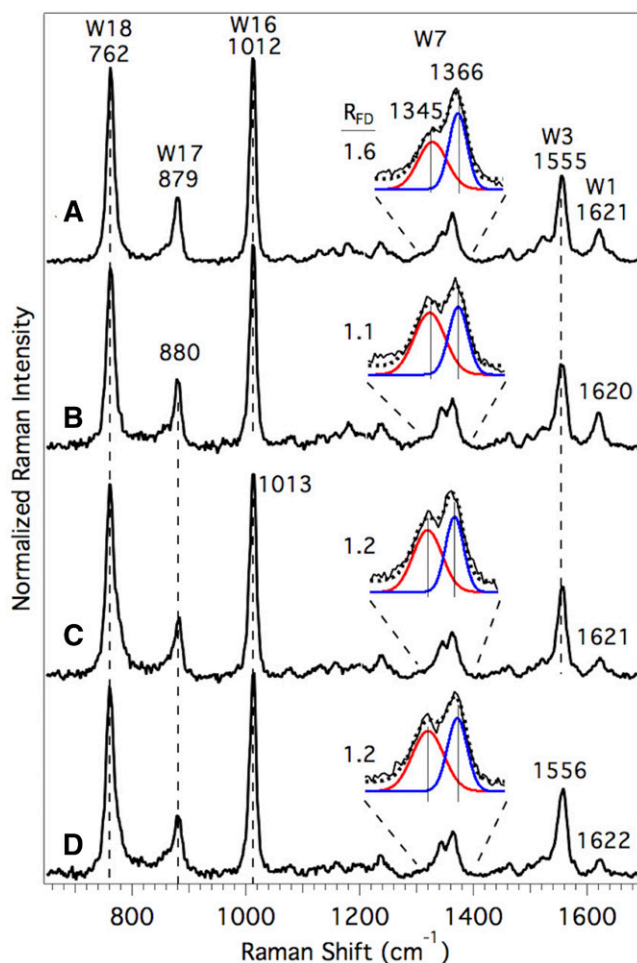


Fig. 9. UVRR spectra of Trp residues in LPL14 in buffer with (A) and without SUVs (B) and model compound NATA in buffer with (C) and without SUVs (D). Spectra were normalized to match the intensity of the W16 band. Concentrations for LPL14 were 9 μM (in buffer) and 11 μM (with SUVs), and for NATA were 32 μM (in buffer) and 33 μM (with SUVs). The excitation wavelength was 228 nm (1.2 mW at the sample). Data were collected for 20 min for each spectrum. Prominent Trp UVRR peaks, including their energies, are labeled. Expanded view of the Fermi doublet region from 1,300 to 1,400 cm^{-1} and the calculated ratio (R_{FD}) of the 1,366 to 1,345 cm^{-1} bands are shown above each spectrum. Gaussian fits to the doublet are shown as red and blue curves, and the sum of the Gaussians is shown as the dashed overlay. The high value of $R_{\text{FD}} = 1.6$ for LPL14 in the presence of SUVs indicates the Trp residue(s) interact with the bilayer.

tryptophans and a phenylalanine) oriented toward the light chain and a polar face (three serines and an aspartic acid) pointing toward the heavy chain. In our crystal structure, a short α -helix was observed in the LPL14 peptide bound to 5D2. However, at this point, it is unclear whether this α -helix is an invariant feature in native LPL or whether it simply represents one of several transient conformations that is detected and then trapped by 5D2 binding. Favoring the latter possibility is the observation that this segment in native LPL (specifically, the peptide FSWSNW) is not protected from deuterium uptake in hydrogen–deuterium exchange studies unless the LPL is bound to Fab 5D2 (9). If the α -helical conformation were an invariant feature of

native LPL, we would have expected to find that the backbone LPL amide hydrogens were protected from deuterium uptake (even in the absence of bound 5D2). The Trp-rich loop in full-length LPL was visualized in a recent cryo-EM LPL structure (20) and appeared to show an α -helical conformation. However, that conformation was presumably a consequence of the repetitive head-to-tail homodimer LPL configuration in the cryo-EM structure, where the Trp-rich loop is buried in the catalytic pocket of a partner LPL molecule. In our X-ray crystal structure of the LPL–GPIHBP1 complex (19), LPL's Trp-rich loop was also buried in the catalytic pocket of a partner LPL molecule and not clearly visualized. In considering the latter structure, there is little reason to believe that GPIHBP1 binding would have changed conformation of the LPL's Trp-rich loop, simply because the Trp-rich loop and the binding site for GPIHBP1 are located on opposite sides of the LPL molecule (19). 5D2 binds avidly to GPIHBP1-bound LPL, as shown in earlier studies (9, 43) and in supplemental Fig. S1 of the current study.


Our studies demonstrated that LPL's Trp-rich loop is a crucial part of the 5D2 epitope, but it is possible that other LPL sequences influence, either directly or indirectly, the strength of 5D2 binding. First, by SPR, 5D2 bound with higher affinity to the carboxyl-terminal region of human LPL (residues 340–475) than to the LPL14 synthetic peptide (9). Second, by SPR, the K_D for 5D2 binding to the human and chicken 14-mer peptides was similar, but by Western blotting, 5D2 binds more avidly to full-length human LPL than to full-length chicken LPL.

Studies by Williams et al. (7) revealed that mutating W420 and W421 in the carboxyl terminus of LPL markedly reduced LPL's ability to bind lipoproteins. Subsequent studies by Lookene et al. (6) revealed that mutating W420 and W421 markedly reduced triglyceride hydrolysis, suggesting that the Trps were either directly involved in binding lipids or that the Trp mutations had simply disrupted LPL conformation. Our current studies support the former possibility. When we incubated LPL14 with SUVs, the peak emission spectra by fluorescence spectroscopy shifted from 358 to 347 nm, whereas no shift occurred when SUVs were added to the model compound NATA. These findings implied direct interactions of the hydrophobic Trp-rich loop with lipids, which is consistent with the fact that Trps often participate in the binding of proteins to membrane bilayers (44). Moreover, UVRR spectra indicated that the Trps in LPL14 interacted directly with lipids. The hydrophobicity of LPL's Trp-rich loop also underlies the propensity of LPL, at high concentrations, to form head-to-tail homodimers (19). In those homodimers, the interaction of the Trp-rich loop with the catalytic pocket shields the hydrophobic Trps from the aqueous environment (19). The binding of 5D2 to LPL also shields the Trp-rich loop and thereby prevents the formation of homodimers (9).

5D2 was generated by immunizing laboratory mice (*Mus musculus*) with bovine LPL. For that reason, it is not particularly surprising that 5D2 does not detect mouse

LPL. Studies of 5D2 binding to LPL peptides indicated that the substitution of a Pro for Ser in the Trp-rich loop of mouse LPL played a role in the absence of 5D2 binding to mouse LPL (2), but it was not clear that this substitution was solely responsible, particularly in the setting of full-length LPL. Our studies settled that issue. When Pro-418 in full-length mouse LPL was changed to Ser, 5D2 bound to mouse LPL avidly, and when Ser-418 in human LPL was replaced with Pro, 5D2 binding to human LPL was abolished. The crystal structure allowed us to make sense of these observations. Replacing Ser-418 with Pro would eliminate the hydrogen bonds and introduce a hydrophobic side chain, which would clash with the side chain of D120 of the 5D2 heavy chain. Interestingly, the Ser-to-Pro substitution in the Trp-rich loop of LPL is found in multiple mouse species (*Mus pahari*, *Mus caroli*, *Mus spicilegus*, and *Mus spretus*) and in the megabat (*Pteropus vampyrus*). By SPR, there was no binding of 5D2 to a synthetic peptide corresponding to the Trp-rich loop from megabat LPL. The appearance of a Pro in the Trp-rich loop in the megabat LPL likely appeared independently during mammalian evolution, as phylogenetic analyses have revealed that bats are more closely related to horses than to mice or humans (45). Interestingly, mice and megabats are both voracious eaters, consuming a large percentage of their body weight each day in food, mainly in the form of carbohydrates. The carbohydrates are likely transformed into triglycerides and used for fuel, but plasma triglyceride levels are low in both mice and the megabat (46, 47). There is no reason to believe that the Pro in the Trp-rich loop interferes with triglyceride hydrolysis. Whether the proline residue in mouse and megabat LPL might actually improve LPL function (e.g., by optimizing LPL's capacity to bind lipids and hydrolyze triglycerides) is unknown.

Data availability

Data are contained in the article. If there are questions, please contact the corresponding authors, Stephen G. Young (e-mail: sgyoung@mednet.ucla.edu; phone: 310-825-4934) and Gabriel Birrane (e-mail: gbirrane@bidmc.harvard.edu; phone: 617-667-0025). As noted in Table 2, the coordinates for APO 5D2 (PDB ID 6WT3) and 5D2-LPL11 (PDB ID 6WN4) have been deposited in the PDB. 

Acknowledgments

The authors thank John Brunzell for sharing the 5D2 hybridoma and Gry Ellis Rasmussen for technical assistance. The authors would like to thank the staff at the AMX beamline 17-ID-1 at the NSLS II, I24 beamline at the Diamond Light Source, and Helix Biostructures for assistance with X-ray data collection.

Author contributions

J.E.K, M.P., S.G.Y., G.B. designed research; J.G.L, A.P.B, D.K.A, C.H., W.S., C.M.A, J.M, Y.T, A.K, T.C., L.G.F performed research; M.M., A.P.B, L.G.F., M.P., G.B. and S.G.Y. analyzed data; S.G.Y. and G.B. wrote the paper.

Funding and additional information

This work was supported by National Heart, Lung, and Blood Institute Grants HL090553, HL087228, and HL125335; Fondation Leducq Transatlantic Network Grant 12CVD04; and Novo Nordisk Foundation Grant NNF17OC0026868. The content is solely the responsibility of the authors and does not necessarily represent the official views of the National Institutes of Health.

Conflict of interest

The authors declare that they have no conflicts of interest with the contents of this article.

Abbreviations

CDR, complement-determining region; GPIHBPI, glycosylphosphatidylinositol-anchored HDL binding protein 1; LPL14, LPL 14-mer peptide ⁴¹⁰KSDSYFSWSDWWSS⁴²³; NATA, N-acetyl tryptophanamide; PDB ID, Protein Data Bank identification number; PFA, paraformaldehyde; RMS, root-mean-square; SPR, surface plasmon resonance; SUV, small unilamellar vesicle; UVRR, UV resonance Raman.

Manuscript received June 20, 2020, and in revised form July 14, 2020. Published, JLR Papers in Press, July 20, 2020, DOI 10.1194/jlr.RA120000993.

REFERENCES

- Babirak, S. P., P. H. Iverius, W. Y. Fujimoto, and J. D. Brunzell. 1989. Detection and characterization of the heterozygote state for lipoprotein lipase deficiency. *Arteriosclerosis*. **9**: 326–334.
- Chang, S-F., B. Reich, J. D. Brunzell, and H. Will. 1998. Detailed characterization of the binding site of the lipoprotein lipase-specific monoclonal antibody 5D2. *J. Lipid Res.* **39**: 2350–2359.
- Peterson, J., W. Y. Fujimoto, and J. D. Brunzell. 1992. Human lipoprotein lipase: relationship of activity, heparin affinity, and conformation as studied with monoclonal antibodies. *J. Lipid Res.* **33**: 1165–1170.
- Wong, H., R. C. Davis, T. Thuren, J. W. Goers, J. Nikazy, M. Waite, and M. C. Schotz. 1994. Lipoprotein lipase domain function. *J. Biol. Chem.* **269**: 10319–10323.
- Liu, M. S., Y. Ma, M. R. Hayden, and J. D. Brunzell. 1992. Mapping of the epitope on lipoprotein lipase recognized by a monoclonal antibody (5D2) which inhibits lipase activity. *Biochim. Biophys. Acta.* **1128**: 113–115.
- Lookene, A., N. B. Groot, J. J. Kastelein, G. Olivecrona, and T. Bruin. 1997. Mutation of tryptophan residues in lipoprotein lipase. Effects on stability, immunoreactivity, and catalytic properties. *J. Biol. Chem.* **272**: 766–772.
- Williams, S. E., I. Inoue, H. Tran, G. L. Fry, M. W. Pladet, P-H. Iverius, J-M. Lalouel, D. A. Chappell, and D. K. Strickland. 1994. The carboxyl-terminal domain of lipoprotein lipase binds to the low density lipoprotein receptor-related protein/ α_2 -macroglobulin receptor (LRP) and mediates binding of normal very low density lipoproteins to LRP. *J. Biol. Chem.* **269**: 8653–8658.
- Goulbourne, C. N., P. Gin, A. Tatar, C. Nobumori, A. Hoenger, H. Jiang, C. R. Grovenor, O. Adeyo, J. D. Esko, I. J. Goldberg, et al. 2014. The GPIHBPI-LPL complex is responsible for the margination of triglyceride-rich lipoproteins in capillaries. *Cell Metab.* **19**: 849–860.
- Kristensen, K. K., K. Z. Leth-Espensen, H. D. T. Mertens, G. Birrane, M. Meiyappan, G. Olivecrona, T. J. D. Jorgensen, S. G. Young, and M. Ploug. 2020. Unfolding of monomeric lipoprotein lipase by ANGPTL4: Insight into the regulation of plasma triglyceride metabolism. *Proc. Natl. Acad. Sci. USA.* **117**: 4337–4346.
- Iverius, P. H., and A. M. Ostlund-Lindqvist. 1976. Lipoprotein lipase from bovine milk. Isolation procedure, chemical characterization, and molecular weight analysis. *J. Biol. Chem.* **251**: 7791–7795.
- Garfinkel, A. S., E. S. Kempner, O. Ben-Zeev, J. Nikazy, S. J. James, and M. C. Schotz. 1983. Lipoprotein lipase: size of the functional unit determined by radiation inactivation. *J. Lipid Res.* **24**: 775–780.
- Olivecrona, T., G. Bengtsson-Olivecrona, J. C. Osborne, Jr., and E. S. Kempner. 1985. Molecular size of bovine lipoprotein lipase as determined by radiation inactivation. *J. Biol. Chem.* **260**: 6888–6891.
- Lookene, A., L. Zhang, M. Hultin, and G. Olivecrona. 2004. Rapid subunit exchange in dimeric lipoprotein lipase and properties of the inactive monomer. *J. Biol. Chem.* **279**: 49964–49972.
- Zhang, L., A. Lookene, G. Wu, and G. Olivecrona. 2005. Calcium triggers folding of lipoprotein lipase into active dimers. *J. Biol. Chem.* **280**: 42580–42591.
- Wang, H., and R. H. Eckel. 2009. Lipoprotein lipase: from gene to obesity. *Am. J. Physiol. Endocrinol. Metab.* **297**: E271–E288.
- Sukonina, V., A. Lookene, T. Olivecrona, and G. Olivecrona. 2006. Angiopoietin-like protein 4 converts lipoprotein lipase to inactive monomers and modulates lipase activity in adipose tissue. *Proc. Natl. Acad. Sci. USA.* **103**: 17450–17455.
- Doolittle, M. H., and M. Peterfy. 2010. Mechanisms of lipase maturation. *Clin. Lipidol.* **5**: 71–85.
- Beigneux, A. P., C. M. Allan, N. P. Sandoval, G. W. Cho, P. J. Heizer, R. S. Jung, K. L. Stanhope, P. J. Havel, G. Birrane, M. Meiyappan, et al. 2019. Lipoprotein lipase is active as a monomer. *Proc. Natl. Acad. Sci. USA.* **116**: 6319–6328.
- Birrane, G., A. P. Beigneux, B. Dwyer, B. Strack-Logue, K. K. Kristensen, O. L. Francone, L. G. Fong, H. D. T. Mertens, C. Q. Pan, M. Ploug, et al. 2019. Structure of the lipoprotein lipase-GPIHBPI complex that mediates plasma triglyceride hydrolysis. *Proc. Natl. Acad. Sci. USA.* **116**: 1723–1732.
- Gunn, K. H., B. S. Roberts, F. Wang, J. D. Strauss, M. J. Borgnia, E. H. Egelman, and S. B. Neher. 2020. The structure of helical lipoprotein lipase reveals an unexpected twist in lipase storage. *Proc. Natl. Acad. Sci. USA.* **117**: 10254–10264.
- Beigneux, A. P., B. S. Davies, S. Tat, J. Chen, P. Gin, C. V. Voss, M. M. Weinstein, A. Bensadoun, C. R. Pullinger, L. G. Fong, et al. 2011. Assessing the role of the glycosylphosphatidylinositol-anchored high density lipoprotein-binding protein 1 (GPIHBPI) three-finger domain in binding lipoprotein lipase. *J. Biol. Chem.* **286**: 19735–19743.
- Leth, J. M., and M. Ploug. 2020. Determination of binding kinetics of intrinsically disordered proteins by surface plasmon resonance. *Methods Mol. Biol.* **2141**: 611–627.
- Kabsch, W. 2010. XDS. *Acta Crystallogr. D Biol. Crystallogr.* **66**: 125–132.
- Tickle, I. J., C. Flensburg, P. Keller, W. Paciorek, A. Sharff, C. Vonrhein, and G. Bricogne. 2018. STARANISO. Global Phasing Ltd., Cambridge, UK. Accessed July 29, 2020, at <http://staraniso.globalphasing.org/>.
- Vonrhein, C., C. Flensburg, P. Keller, A. Sharff, O. Smart, W. Paciorek, T. Womack, and G. Bricogne. 2011. Data processing and analysis with the autoPROC toolbox. *Acta Crystallogr. D Biol. Crystallogr.* **67**: 293–302.
- McCoy, A. J., R. W. Grosse-Kunstleve, P. D. Adams, M. D. Winn, L. C. Storoni, and R. J. Read. 2007. Phaser crystallographic software. *J. Appl. Crystallogr.* **40**: 658–674.
- Burak, M. F., K. E. Inouye, A. White, A. Lee, G. Tuncman, E. S. Calay, M. Sekiya, A. Tirosh, K. Eguchi, G. Birrane, et al. 2015. Development of a therapeutic monoclonal antibody that targets secreted fatty acid-binding protein ap2 to treat type 2 diabetes. *Sci. Transl. Med.* **7**: 319ra205.
- Liebschner, D., P. V. Afonine, M. L. Baker, G. Bunkoczi, V. B. Chen, T. I. Croll, B. Hintze, L. W. Hung, S. Jain, A. J. McCoy, et al. 2019. Macromolecular structure determination using X-rays, neutrons and electrons: recent developments in Phenix. *Acta Crystallogr. D Struct. Biol.* **75**: 861–877.
- Otwinowski, Z., and W. Minor. 1997. Processing of X-ray diffraction data collected in oscillation mode. *Methods Enzymol.* **276**: 307–326.
- Vagin, A., and A. Teplyakov. 2010. Molecular replacement with MOLREP. *Acta Crystallogr. D Biol. Crystallogr.* **66**: 22–25.
- Cowtan, K. 2006. The Buccaneer software for automated model building. 1. Tracing protein chains. *Acta Crystallogr. D Biol. Crystallogr.* **62**: 1002–1011.
- Emsley, P., B. Lohkamp, W. G. Scott, and K. Cowtan. 2010. Features and development of Coot. *Acta Crystallogr. D Biol. Crystallogr.* **66**: 486–501.

33. Murshudov, G. N., A. A. Vagin, and E. J. Dodson. 1997. Refinement of macromolecular structures by the maximum-likelihood method. *Acta Crystallogr. D Biol. Crystallogr.* **53**: 240–255.
34. Williams, C. J., J. J. Headd, N. W. Moriarty, M. G. Prisant, L. L. Videau, L. N. Deis, V. Verma, D. A. Keedy, B. J. Hintze, V. B. Chen, et al. 2018. MolProbity: More and better reference data for improved all-atom structure validation. *Protein Sci.* **27**: 293–315.
35. Pace, C. N., F. Vajdos, L. Fee, G. Grimsley, and T. Gray. 1995. How to measure and predict the molar absorption coefficient of a protein. *Protein Sci.* **4**: 2411–2423.
36. Asamoto, D. K., and J. E. Kim. 2019. UV resonance Raman spectroscopy as a tool to probe membrane protein structure and dynamics. *Methods Mol. Biol.* **2003**: 327–349.
37. Krissinel, E., and K. Henrick. 2004. Secondary-structure matching (SSM), a new tool for fast protein structure alignment in three dimensions. *Acta Crystallogr. D Biol. Crystallogr.* **60**: 2256–2268.
38. Winn, M. D., C. C. Ballard, K. D. Cowtan, E. J. Dodson, P. Emsley, P. R. Evans, R. M. Keegan, E. B. Krissinel, A. G. Leslie, A. McCoy, et al. 2011. Overview of the CCP4 suite and current developments. *Acta Crystallogr. D Biol. Crystallogr.* **67**: 235–242.
39. Krissinel, E., and K. Henrick. 2007. Inference of macromolecular assemblies from crystalline state. *J. Mol. Biol.* **372**: 774–797.
40. Maupetit, J., P. Derreumaux, and P. Tuffery. 2010. A fast method for large-scale *de novo* peptide and miniprotein structure prediction. *J. Comput. Chem.* **31**: 726–738.
41. Bailey, J. E., G. H. Beaven, D. A. Chignell, and W. B. Gratzer. 1968. An analysis of perturbations in the ultraviolet absorption spectra of proteins and model compounds. *Eur. J. Biochem.* **7**: 8–14.
42. Kang, G., I. López-Peña, S. Bhakta, and J. E. Kim. 2013. Probing membrane protein structure and dynamics by fluorescence spectroscopy. In *Encyclopedia of Analytical Chemistry: Applications, Theory and Instrumentation*. John Wiley & Sons, Ltd., Accessed July, 29, 2020, at <https://onlinelibrary.wiley.com/doi/abs/10.1002/9780470027318.a9353>.
43. Allan, C. M., M. Larsson, X. Hu, C. He, R. S. Jung, A. Mapar, C. Voss, K. Miyashita, T. Machida, M. Murakami, et al. 2016. An LPL-specific monoclonal antibody, 88B8, that abolishes the binding of LPL to GPIHBP1. *J. Lipid Res.* **57**: 1889–1898.
44. Sanchez, K. M., G. Kang, B. Wu, and J. E. Kim. 2011. Tryptophan-lipid interactions in membrane protein folding probed by ultraviolet resonance Raman and fluorescence spectroscopy. *Biophys. J.* **100**: 2121–2130.
45. Zhang, G., C. Cowled, Z. Shi, Z. Huang, K. A. Bishop-Lilly, X. Fang, J. W. Wynne, Z. Xiong, M. L. Baker, W. Zhao, et al. 2013. Comparative analysis of bat genomes provides insight into the evolution of flight and immunity. *Science*. **339**: 456–460.
46. Heard, D. J., M. M. Ruiz, and K. E. Harr. 2006. Comparison of serum and plasma for determination of blood biochemical values in Malaysian flying foxes (*Pteropus vampyrus*). *J. Zoo Wildl. Med.* **37**: 245–248.
47. Otto, G. P., B. Rathkolb, M. A. Oestereicher, C. J. Lengger, C. Moerth, K. Micklich, H. Fuchs, V. Gailus-Durner, E. Wolf, and M. Hrabe de Angelis. 2016. Clinical Chemistry Reference Intervals for C57BL/6J, C57BL/6N, and C3HeB/FeJ Mice (*Mus musculus*). *J. Am. Assoc. Lab. Anim. Sci.* **55**: 375–386.
48. Fenn, T. D., D. Ringe, and G. A. Petsko. 2003. POVScript+: a program for model and data visualization using persistence of vision ray-tracing. *J. Appl. Crystallogr.* **36**: 944–947.